Self-recovery Superhydrophobic Surfaces: Modular Design

Emanuele Lisi, Matteo Amabili, Simone Meloni,* Alberto Giacomello,* and Carlo Massimo Casciola

Dipartimento di Ingegneria Meccanica e Aerospaziale, Università di Roma "La Sapienza", Rome, Italy

E-mail: simone.meloni@uniroma1.it; alberto.giacomello@uniroma1.it

November 1, 2017

Abstract

Superhydrophobicity, the enhanced hydrophobicity of surfaces decorated with textures of suitable size, is associated with a layer of gas trapped within surface roughness. The reduced liquid/solid contact makes superhydrophobicity attractive for many technological applications. This gas layer, however, can break down with the liquid completely wetting the surface. Experiments have shown that the recovery of the "suspended" superhydrophobic state from the wet one is difficult. Self-recovery – the spontaneous restoring of the gas layer at ambient conditions – is one of the dreams of research in superhydrophobicity as it would allow to overcome the fragility of superhydrophobicity.

In this work we have performed a theoretical investigation of the wetting and recovery processes on a set of surfaces characterized by textures of different dimensions and morphology in order to elucidate the optimal parameters for avoiding wetting and achieving self-recovery. Results show that texture size in the nanometer range is a

necessary condition for self-recovery, but not a sufficient one: the geometry plays a crucial role – nanopillars prevent self-recovery while surfaces with square pores exhibit self-recovery even at large positive pressures. However, the optimal morphology for self-recovery, the square pore, is sub-optimal for the functional properties of the surface, e.g., high slippage. Our calculations show that these properties are related to regions of the texture separated in space: self-recovery is controlled by the characteristics of the bottom surface while wetting and slip by the cavity mouth. We thus propose a modular design strategy which combines self-recovery and good functional properties: square pores surmounted by ridges achieve self-recovery even at 2 MPa and have a very small liquid/solid contact area. The macroscopic calculations, which allowed us to efficiently devise design criteria, have been validated by atomistic simulations, with the optimal texture showing self-recovery on atomic timescales, $\tau \sim 2$ ns.

Keywords

Superhydrophobicity, wetting, self-recovery, free energy simulations, sharp interface model, molecular dynamics

Superhydrophobic surfaces are textured surfaces made of hydrophobic materials. A liquid in contact with such surfaces can be suspended over a gas layer entrapped in the cavities by capillary forces: the Cassie-Baxter state[1] (CB, Fig. 1a). The reduced contact area with the solid makes the superhydrophobic Cassie-Baxter state suitable for self-cleaning,[2,3] anti-icing,[4–6] humidity-proof coatings,[7,8] microcondensation,[9] drag-reduction,[10–12] oil-water separation,[13–15] superhydrophobic electrodes for batteries and fuel cells,[16–18] prevention of corrosion,[19,20] and other technological applications. On the same surface and under the same conditions a liquid might also completely wet the textures; in this case the system is said to be in the Wenzel state[21] (W, Fig. 1b), which is characterized by very large liquid/solid contact area. The superhydrophobic properties of textured surfaces are related to the intervening gas layer (CB state). For this reason, one should speak of superhydrophobic states

rather than superhydrophobic surfaces.

In typical applications, Cassie-Baxter and Wenzel are two stable or metastable states of the system. A surface prepared in the metastable state, e.g., Cassie-Baxter, can remain in the initial configuration for long timescales, which depend on the thermodynamic conditions and on the texture characteristics. It is clear that in most applications the transition from the Cassie-Baxter to the Wenzel state should be delayed or avoided. At the same time, it is desirable to favor the reverse transition from the Wenzel to the Cassie-Baxter state – the recovery of superhydrophobicity – should the system undergo wetting due, for example, to a temporary change of external conditions. The aim of the present work is to design the geometry and morphology of surface textures in order to realize surfaces that cannot be wetted under normal conditions and, even when this happens, they are capable of rapidly recovering without external inputs.

A thought experiment in which the pressure is increased from ambient conditions and subsequently restored can help understanding the problem of wetting and recovery in more rigorous terms, following the equilibrium arguments of, e.g., Refs.[22,23] At ambient conditions the free energy of the system presents two minima (Fig. 1c): an absolute minimum – the stable state, Cassie-Baxter in the hypothesis – and a local minimum – the metastable Wenzel state – separated by a free-energy barrier $\Delta\Omega^{\dagger}_{\mathrm{CW}}$. Thus, if this specific system is initially prepared in the Cassie-Baxter state it remains in this state. When the pressure increases, the difference of free energy $\Delta\Omega_{\mathrm{CW}} = \Omega_{\mathrm{C}} - \Omega_{\mathrm{W}}$ between the Cassie-Baxter and Wenzel states increases from negative values. Eventually, $\Delta\Omega_{\mathrm{CW}}$ becomes zero at the heterogeneous coexistence pressure P^{co} (Fig. 1d), and positive for $P > P^{\mathrm{co}}$ (Fig. 1e). At moderate pressures the barrier separating the Cassie-Baxter and Wenzel states, $\Delta\Omega^{\dagger}_{\mathrm{CW}}$, is much larger than the thermal energy available to the system, $k_{\mathrm{B}}T$, where k_{B} is the Boltzmann constant and T the temperature. Thus, the transition time $\tau = \tau_0 \exp(\Delta\Omega^{\dagger}_{\mathrm{CW}}/k_{\mathrm{B}}T)$[24,25] is longer than the experimental time of observation. Therefore, the system remains kinetically trapped in the Cassie-Baxter state even when this is metastable. Upon additional increase of the pressure,

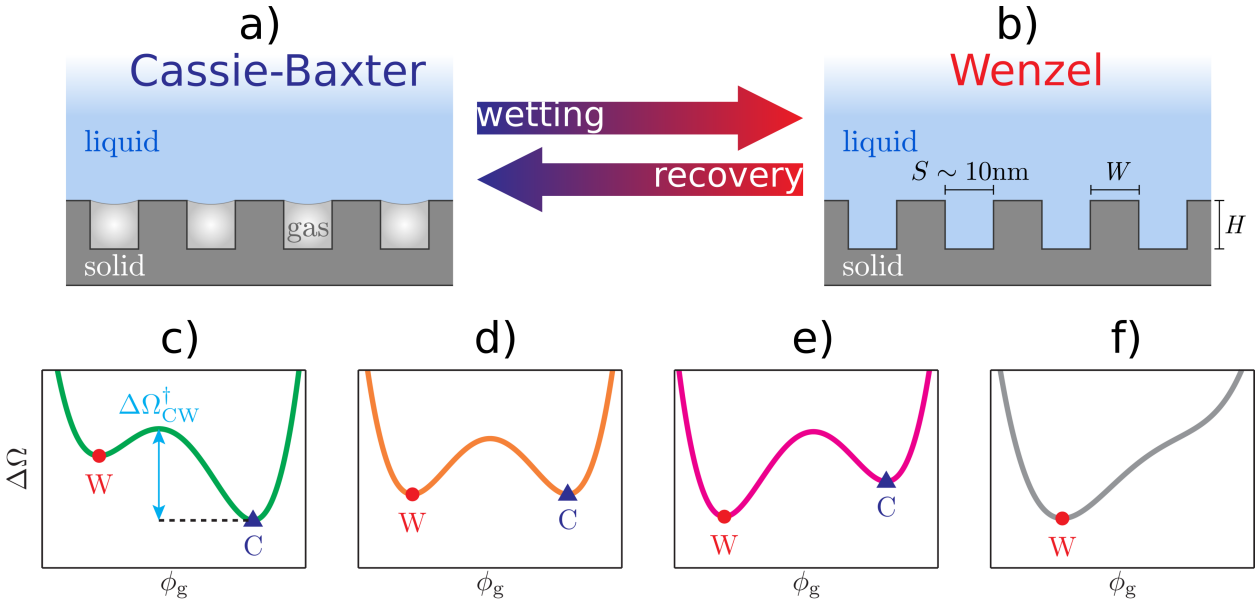

Figure 1: Cartoon illustrating the configuration of the Cassie-Baxter (a) and Wenzel (b) states, the (meta)stable states of a system consisting of a liquid (l) and gas (g) in contact with a solid surface (s) with (simple) textures. In the panel (b) are illustrated the characteristic dimensions of the surface textures considered in the present work: the thickness W, the spacing (pitch) S and the height H. Panels (c-f) report the cartoon of energy profiles along the wetting/recovery process at various pressures (pressure increases in going from panel c to f). At low pressure (c) Cassie-Baxter is stable and Wenzel is metastable. Increasing the pressure the heterogeneous coexistence is achieved (d) at which the two states (minima) have the same free energy. Further increasing the pressure Wenzel becomes the stable state (e), but the two states are still separated by a large barrier, much higher than the thermal energy. Finally, at large pressures there is no minimum in correspondence of the Cassie-Baxter state: Wenzel is the only stable state available to the system.

the barrier decreases until it becomes small enough that the system can readily undergo the Cassie-Baxter/Wenzel transition (Fig. 1f). If the initial external conditions are restored, the recovery barrier $\Delta\Omega^{\dagger}_{WC}$ is very large, the system remains kinetically trapped in the Wenzel state (Fig. 1b) and recovery cannot be achieved. This thought experiment illustrates why several experimental and theoretical works[22,23,26] report that the Cassie-Baxter/Wenzel transition is irreversible for standard surfaces operating near ambient conditions.

Several strategies have been developed to preserve[27–30] or recover[31–33] the Cassie-Baxter state. Hierarchical surfaces have been fabricated to increase the intrusion pressure, but no quantitative design criteria have been identified yet to fabricate optimal systems. *Active*

approaches to enhance wetting resistance have also been considered, such as pressurization of the gas layer ,[28,29] but this adds complexity to the system. Concerning the recovery, several strategies have been developed, including the *in situ* development (and spread) of gas,[31] electrical switching,[32,34] mechanical vibration,[33] but also these approaches add complexity to the system.

Ideally, a superhydrophobic surface should be able to withstand the highest possible pressure without undergoing a wetting transition[22,23,35–41] and recover the Cassie-Baxter state once the perturbation has ceased (self-recovery). Pioneering attempts to design surfaces with these characteristics were based on heuristic hypotheses on the Cassie-Baxter/Wenzel transition mechanism.[42–46] More recently, Prakash *et al.*[47] have proposed the modification of the internal part of nano-pillar surfaces by a sphere of hydrophobic material to enhanced the resistance to the wetting and promote the recovery. A possible drawback of this approach is that the hydrophobic sphere necessary to make the recovery barrier negligible occupies most of the surface cavities, which might affect the function of the surface. Giacomello *et al*[48] have shown that self-recovery can be achieved even at large pressures, if the surface textures have the characteristic size of 2 nm or less; the precise dimension depends on the contact angle of the surface. Here, building upon these early attempts we identify design principles of self-recovery surfaces which do not affect their functional properties.

To achieve our objectives we first consider a number of surfaces with textures of technological interest and investigate their properties with respect to liquid intrusion and extrusion. In particular, we focus on surfaces decorated with circular and square pores, square pillars, and ridges of nanoscopic size (Fig. 2a-d). We investigate the dependence on the liquid pressure of the wetting and recovery barriers for these systems. From this analysis one identifies the fundamental design principles affecting the resistance to wetting and self-recovery abilities. Second, on the basis of the wetting properties of simple texture morphologies we design surfaces combining good superhydrophobic characteristics, robustness of the Cassie-Baxter state, and self-recovery properties (Fig. 2e-f). For our best surface, we also identify the max-

imum possible size of the texture that still allows self-recovery, which is a key fabrication parameter.

The present analysis is based on a combined macro- and microscopic approach. The wetting and recovery mechanism and barrier of the extended set of systems is studied by the continuum rare events method – CREaM[36]– which allows to identify transition barriers for a liquid in a complex confining environment based on the sharp interface model of a solid-liquid-gas system. For selected systems, results are validated by *standard* (MD) and by restrained molecular dynamics (RMD),[49,50] a simulation technique designed to compute the free-energy profile of systems characterized by large free-energy barriers.

Anticipating our results, we show that the recovery barrier is essentially determined by the morphology and geometrical characteristics of the bottom of the corrugations, while the wetting barrier is mainly associated with the characteristics of the top part of the textures. It turns out that the most efficient topography for self-recovery is the surface with square nanopores, which, however, typically has a large liquid/solid contact area, resulting in unsatisfactory superhydrophobic properties. Moreover, in square-pore surfaces one of the walls of the textures is orthogonal to the flow, with potential limitations to the drag reduction. Pillar and ridge surfaces, on the contrary, present lower liquid/solid contact areas and perform better at reducing drag,[51] but their recovery barrier is very large making the wetting process typically irreversible. These observations brought us to propose a modular design of textured surfaces consisting of the combination of simple texture morphologies of the kinds listed above. In particular, we have found that the combination of ridges and square pores, resulting in a topography of ridge textures with transversal bulkheads at their bottom, renders surfaces highly resistant to wetting, capable of self-recovery, and retaining the good superhydrophobic properties of ridges.

Results and Discussion

We study the thermodynamics and kinetics of the wetting and recovery by considering the grand potential Ω of the system as a function of the volume of gas $V_{\rm g}$ in the surface corrugations. This grand potential profile is obtained from a macroscopic model of the three-phase solid-liquid-gas system as explained in the *Methods* section. From the grand potential profile (Fig. 1c-e) one obtains the wetting $\Delta\Omega^{\dagger}_{\rm CW}$ and recovery $\Delta\Omega^{\dagger}_{\rm WC}$ barriers at different pressures. In the present work we take as the operative definition of intrusion pressure, $P^{\rm int}$ (extrusion pressure, $P^{\rm ext}$), the pressure at which the wetting (recovery) barrier is $25k_{\rm B}T$, corresponding to a transition time $\tau = \tau_0 \exp(\Delta\Omega^{\dagger}/k_{\rm B}T) = 1$ s,[25] i.e., the order of magnitude of the typical experimental time. From Ω one obtains also the coexistence pressure $P^{\rm co}$ for the heterogeneous system, i.e., the pressure at which the Cassie-Baxter and Wenzel states have the same grand potential (Fig. 1d).

The three-phase system is described in terms of the sharp interface model, consisting of solid, liquid, and gas bulk domains separated by sharp discontinuities at their interfaces. The corresponding grand potential is the sum of bulk and interface terms: $\Omega = -P_{\rm s}V_{\rm s} - P_{\rm l}V_{\rm l} - P_{\rm g}V_{\rm g} + \gamma_{\rm sl}A_{\rm sl} + \gamma_{\rm lg}A_{\rm lg} + \gamma_{\rm sg}A_{\rm sg}$, where P_x and V_x are the pressure and volume of a generic phase x and γ_{xy} and A_{xy} are the surface tension and area between the x and y phases, respectively. Considering that the solid surface does not change during the process, the state of the system is fully characterized by the liquid/gas interface –the meniscus– whose intersection with the solid surface determines the volume of each phase and the areas of the various interfaces. The (relative) grand potential can be recast into the more convenient form:

$$\Delta\Omega = \Delta P V_{\rm g} + \gamma_{\rm lg}(A_{\rm lg} + \cos\theta_Y A_{\rm sg}) \tag{1}$$

where the Young contact angle $\cos\theta_{\rm Y} = (\gamma_{\rm sg} - \gamma_{\rm sl})/\gamma_{\rm lg}$ depends on the chemical nature of the solid, liquid, and gas and $\Delta P = P_{\rm l} - P_{\rm g}$ is the difference between the pressure of the liquid and the gas. Within the sharp-interface approximation, in which surface tension terms do not

depend on the pressure, for a given surface morphology and chemistry, ΔP determines the relative stability of the Cassie-Baxter and Wenzel states. For convenience, in the following we will report Ω as a function the gas volume fraction $\phi_g = V_g/V_T$, where V_T is the volume of the texture cavities.

The wetting and recovery processes can proceed with the liquid entering into or exiting from the textures along different trajectories. By trajectory we mean the sequence of meniscus configurations along the wetting/recovery, i.e., as a function of ϕ_g. Different paths are characterized by different grand potential profiles which correspond to different meniscus morphologies along the process and, thus, to different values of the interface terms in Eq. (1). Among these trajectories, we consider that of maximum probability as identified by the continuum rare event method (CREaM – described in the *Methods* section), and along it we compute Ω (see Supp. Info. for a discussion on wetting *via* the depinning *vs* sagging mechanisms). θ_Y is set to 125°, corresponding to the *state of the art* hydrophobic materials,[52,53] and $\gamma_{lg} = 0.072\, N/m$, i.e., the surface tension of water at room temperature.

We first consider the wetting/recovery characteristics of four basic types of textures of interest for technological applications: i) circular and ii) square pores, iii) pillars and iv) ridges (Fig. 2a-d). The geometry of these textures is characterized by three parameters: the spacing (S), the thickness (W), and the height (H) of the solid part of the corrugations (Fig. 1b). The detailed study of how these three geometrical parameters affect the relative stability of the Cassie-Baxter *vs* Wenzel state, the wetting and recovery barriers, the intrusion and extrusion pressure, and their dependence on the temperature will be discussed in a forthcoming article. Here we focus on the analysis and design of textures in a range allowing for self-recovery. In particular, we consider textures of thickness $W = 1$ nm, with S and H chosen such that the cross section and volume of the texture are 121 nm^2 and 1100 nm^3, respectively ($S \sim H \sim 10$ nm). As we will discuss more in detail below, this size is in the range allowing self-recovery at ambient conditions.

In Fig. 2a-d we report the grand potential as a function of the amount of gas in the

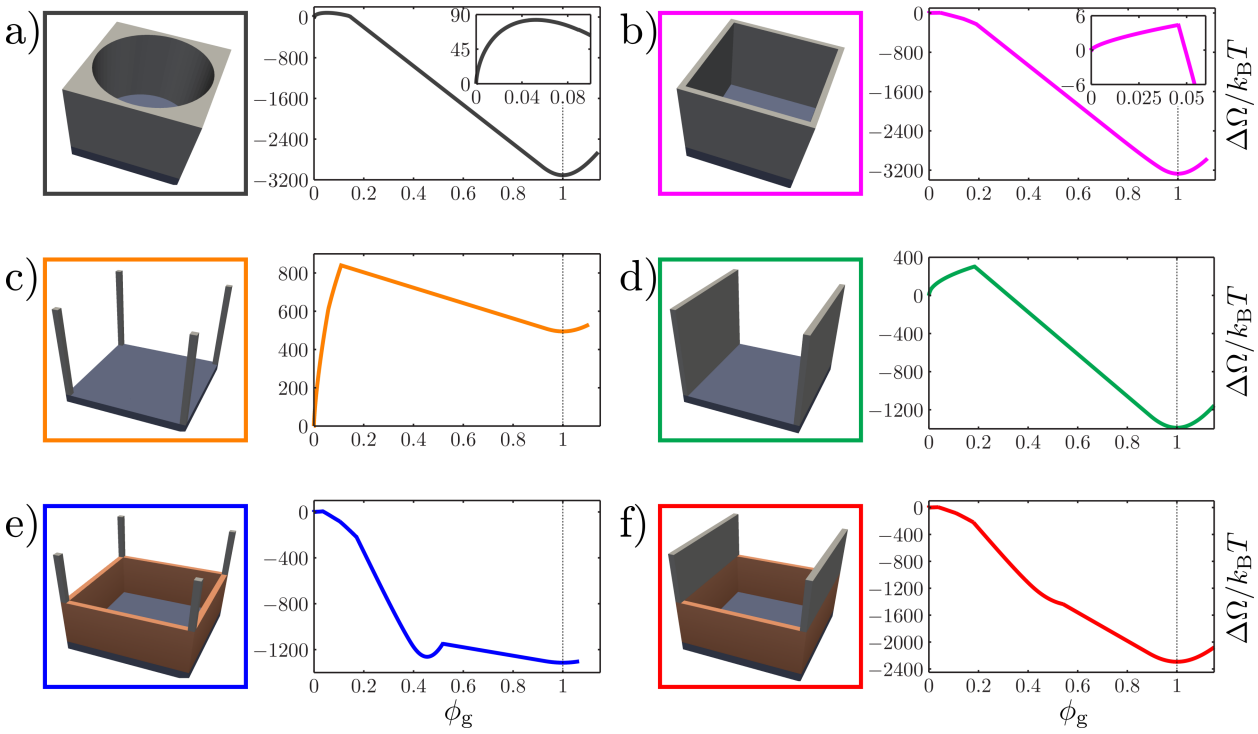

Figure 2: Surface textures considered in this work together with grand-potential profiles expressed in k_BT units as function of gas volume fraction (ϕ_g) in the cavities at ambient conditions ($\Delta P \approx 0.1$ MPa). a) Circular and b) square pores, c) pillars, d) ridges. The final panels show the proposed modular textures: e) square pores/pillars and f) square pores/ridges.

cavities at ambient conditions. The shape of these curves is qualitatively similar, with two minima corresponding to the Cassie-Baxter and Wenzel states separated by a barrier. For all but the pillar system the grand potential of the Cassie-Baxter state is lower than the Wenzel one, i.e., Cassie-Baxter is stable and Wenzel is metastable. For the pillars the order of stability between the two wetting states is opposite because of the small hydrophobic surface area of the thin structures considered in the present work; thicker pillars (higher W) or a smaller pitch (lower S) will eventually result in a stabilization of the Cassie-Baxter over Wenzel state. Nevertheless, even when the Cassie-Baxter state is metastable, due to the large wetting barrier and the correspondingly long transition time (Table 2), a droplet deposited on the pillar surface or the surface immersed in a liquid will remain in the superhydrophobic state for experimentally relevant times.

We remark that all the systems considered have a high intrusion pressure due to their

Table 1: Characteristics of the textured surfaces considered in the present work; P^{co} is the heterogeneous coexistence pressure, $\Delta\Omega^{\dagger}$ is the corresponding wetting and recovery barrier. For the modular structures (pore/pillars and pore/ridges) P^{co} is the coexistence pressure between the Wenzel and the *intermediate* Cassie-Baxter (iC) state: there is no pressure at which Wenzel and Cassie-Baxter have the same Ω for these surfaces. P^{int} and P^{ext} are the intrusion and extrusion pressures at room temperature, respectively. As explained in the text, the operative definition of intrusion and extrusion pressure is the pressure at which the corresponding barrier is $25\,k_{\mathrm{B}}T$. For modular structures, in which the system presents three (meta)stable states, P^{int} and P^{ext} are determined by the largest of the two iC/C and iC/W barriers. In particular, for both modular surfaces the intrusion pressure is the one at which $\Delta\Omega^{\dagger}_{\mathrm{iCW}} = 25\,k_{\mathrm{B}}T$. Concerning the extrusion pressure, the relevant barrier is $\Delta\Omega^{\dagger}_{\mathrm{iCC}}$ for the square pore/pillar surface and $\Delta\Omega^{\dagger}_{\mathrm{WiC}}$ for the square pore/ridge one. The solid fraction f and the corresponding apparent contact angle θ for a system in the Cassie-Baxter state are also reported.

	P^{co} $[MPa]$	$\Delta\Omega^{\dagger}$ $[k_{\mathrm{B}}T]$	P^{int} $[MPa]$	P^{ext} $[MPa]$	f	θ $[^{\circ}]$
a) Circular pore	12.6	476	14.9	-9.4	0.24	154
b) Square pore	13.9	421	16.4	1.8	0.17	158
c) Pillars	-1.6	788	1.3	-52.7	0.01	175
d) Ridges	5.4	568	8.1	-17.8	0.09	164
e) Square pore/pillars	11.0	283	15.7	-7.14	0.01	175
f) Square pore/ridges	11.1	289	15.7	2.0	0.09	164

Table 2: Wetting and recovery characteristics of *standard* and modular surfaces at ambient conditions: wetting, $\Delta\Omega^{\dagger}_{\mathrm{CW}}$, and recovery, $\Delta\Omega^{\dagger}_{\mathrm{WC}}$, barriers and corresponding times, τ_{CW} and τ_{WC}. At ambient conditions the modular square pore/pillars surface has three (meta)stable states. Thus, the overall wetting and recovery processes are characterized by two barriers each and the associated transition times, corresponding to the C→iC and iC→W (left and right numbers of the slash), and W→iC and iC→C, respectively.

	$\Delta\Omega^{\dagger}_{\mathrm{CW}}$ $[k_{\mathrm{B}}T]$	τ_{CW} $[s]$	$\Delta\Omega^{\dagger}_{\mathrm{WC}}$ $[k_{\mathrm{B}}T]$	τ_{WC} $[s]$
a) Circular pore	3169	$2 \cdot 10^{1365}$	84	$5 \cdot 10^{25}$
b) Square pore	3254	$1 \cdot 10^{1402}$	5.7	$3 \cdot 10^{-9}$
c) Pillars	320	$1 \cdot 10^{128}$	843	$2 \cdot 10^{355}$
d) Ridges	1671	$6 \cdot 10^{714}$	309	$1 \cdot 10^{123}$
e) Square pore/pillars	152.5/1257	$2 \cdot 10^{55}/3 \cdot 10^{534}$	6.5/115.5	$7 \cdot 10^{-9}/1 \cdot 10^{39}$
f) Square pore/ridges	2274	$6 \cdot 10^{976}$	6.3	$6 \cdot 10^{-9}$

reduced size; among those, the pore surfaces, in particular the square pore, can better resist to intrusion. The superior ability of pore surface to resist to intrusion can be intuitively understood considering that the driving force of the wetting, $\Delta P V_{\mathrm{g}}$, which is the same for all systems, is opposed by the solid/liquid-solid/gas surface term, $\gamma_{\mathrm{lg}} \cos\theta_Y A_{\mathrm{sg}}$, which is

maximum in the square pore case.

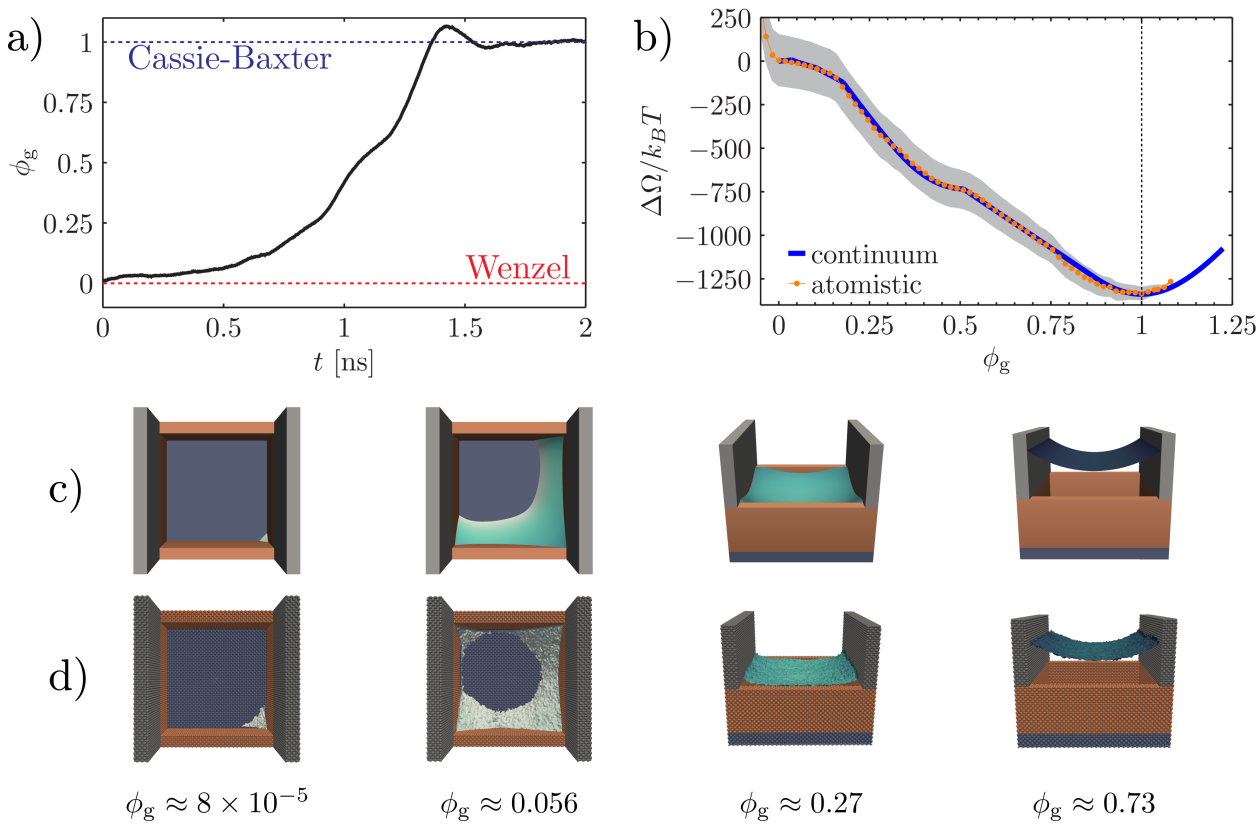

Figure 3: a) Gas volume fraction as a function of time along a MD starting from the Wenzel state at ambient conditions for the square pore/ridge surface. Complete recovery is achieved within 1.5 ns. b) Comparison between the atomistic and continuum grand potential; continuum data has been obtained without any fitting of atomistic results. The gray area represents the confidence interval associated to the determination of the atomistic Ω profile. c) and d) are selected meniscus configurations observed along recovery in continuum and atomistic simulations, respectively, at corresponding ϕ_g values.

Upon large pressure variations such that $P \geq P^{\text{int}}$, caused, e.g., by impact[54] or evaporation[37] of a water droplet, or turbulence in submerged applications,[55] the system readily undergoes a Cassie-Baxter/Wenzel transition. Experiments show that typically when the external perturbation triggering the transition terminates, e.g., if the pressure perturbation decreases, the system remains in the Wenzel state, i.e., the transition is irreversible.[22] The reason is that in the original conditions, typically ambient pressure and temperature, the recovery barrier is very large. This is the case of the nanoscopic pillar and ridge surfaces considered in this work (Fig. 2c-d), which at ambient conditions present recovery barriers of 840

and 309 $k_{\mathrm{B}}T$, respectively, corresponding to recovery times $\tau_{\mathrm{WC}} \sim 10^{355}$ and $\tau_{\mathrm{WC}} \sim 10^{123}$ s (Table 2). The recovery barrier is much lower in the case of circular and square pores. In particular, in the case of the square pore the recovery barrier at ambient conditions is $\Delta\Omega^{\dagger}_{\mathrm{WC}} = 5.7\ k_{\mathrm{B}}T$ and recovery time $\tau_{\mathrm{WC}} = 3 \cdot 10^{-9}\ s$; in other words: nanoscale square-pore surfaces are capable of self-recovery at ambient conditions. Actually, our calculations show that nanoscopic square pore surfaces are able of self-recovery also at positive pressures, up to $P^{\mathrm{ext}} \sim 1.8$ MPa (Table 1). The extrusion pressures of the four systems follows the ordering *square pore* > *circular pore* > *ridges* > *pillars* (Table 1). In particular square pores are the only system with a positive P^{ext}. These results show that nanocorrugations are necessary but not sufficient for self-recovery: the morphology of textures crucially affects the recovery barrier and extrusion pressure.

The relation between $\Delta\Omega^{\dagger}_{\mathrm{WC}}$, P^{ext}, and the morphology of the textures can be understood noticing that the configuration of the system at the transition state – the maximum of the grand potential– is a gas bubble at the intersection between the solid part of the textures and the bottom wall (Fig. 2). The gas bubble is formed at this place because here the highest ratio $\chi = A_{\mathrm{sg}}/A_{\mathrm{lg}}$ is achieved. According to the sharp-interface model of Eq. (1) the denominator is associated to the energy penalty of forming a liquid/gas interface, $\gamma_{lg}A_{lg}$, and the numerator to the energy gain of heterogeneous nucleation at an hydrophobic surface, $\gamma_{lv}\cos\theta_Y A_{sg}$, ($\cos\theta_Y < 0$ for hydrophobic surfaces); the value of this ratio is maximum for a bubble located at the intersection between the vertical and the bottom walls of the cavity, which is where nucleation takes place. In addition, for a bubble of prescribed volume, e.g., the volume of the critical bubble of the square pore, this ratio is higher in the square pore ($\chi = 1.73$), followed by the circular pore ($\chi = 1.46$), the ridge ($\chi = 1.41$) and, finally, the pillars ($\chi = 0.97$).

Summarizing: all the nanotextured surfaces analyzed here are able to resist to intrusion under the action of intense pressures, with $P^{\mathrm{int}} \in [1.28, 16.37]$ MPa; the pore surface emerges as the best one at resisting intrusion and at achieving recovery, with those decorated with

square pores being able to self-recover at positive pressures.

One might be tempted to consider the square pore surface optimal for superhydrophobic applications. However, it must be remarked that for a prescribed thickness W pore surfaces have a much higher solid fraction f (Table 1) – the ratio between the solid surface wet by the liquid in the Cassie-Baxter state A_{wet} over the nominal surface A_{nominal} – which might affect their *functional* properties. For example, the apparent contact angle θ is an important parameter to characterize emerged applications of superhydrophobicity, i.e., those involving a rough surface immersed in air and in contact with liquid drops: typically, the higher θ the better is the surface at repelling drops. In the Cassie-Baxter state the apparent contact angle is given by[1] $\cos\theta = f(\cos\theta_Y + 1) - 1$, where f is the solid fraction. Thus, for a given surface chemistry, encoded by θ_Y, the emerged superhydrophobicity, θ, increases with decreasing solid fraction. The apparent contact angle of the four surfaces considered here is $\theta_{\text{circular}} = 154°$, $\theta_{\text{square}} = 158°$, $\theta_{\text{ridges}} = 164°$ and $\theta_{\text{pillars}} = 175°$. A quantitative comparison for the effect of morphology on drag is more complex but experimental and theoretical works have shown that pillars and ridge surfaces are better suited for these applications than the others considered here. For instance, Ref.[51] numerically investigates the case of laminar flows, predicting slip lengths of 30 nm for pillars, 7 nm for ridges, and 2 nm for square pores with the same f as the present work. For turbulent flows, ridges perform best among the investigated textures.[10] Our results suggest that a single elementary texture is unable to satisfy all the requirements of superhydrophobic surfaces: resistance to wetting, self-recovery, high contact angle and/or low drag, etc.

Here we propose a modular design for achieving optimal characteristics for emerged and submerged applications of superhydrophobic surfaces. This approach consists in combining two texture morphologies with the same characteristic length on the same surface: a square pore combined with pillars or with ridges (Fig. 2e-f). This approach is inspired by the observation that the regions of the textures responsible for the recovery and that for the functional properties of the surface are separated in space: recovery is determined by the

morphology and geometry of the bottom while functional properties are controlled by the characteristics of the top of corrugations, i.e., by the cavity mouth. In particular, since the recovery transition state consists of a small bubble at one of the bottom corners of the pore ($\phi_g = 0.046$, Fig. 2b), a shallow pore is sufficient to induce self-recovery. Thus, the idea is to install pillars or ridges on top of the pore to obtain a modular surface with, at the same time, optimal functional and recovery properties. The two modular surfaces we consider have the same overall height of the pillar and ridge surfaces, with the bottom half consisting of the square pore and the top half of pillars or ridges.

In the modular surfaces one might observe the formation of a new (meta)stable state, that we denote as *intermediate* Cassie-Baxter (iC); this state corresponds to a configuration in which the meniscus is pinned at the top of the square pore, see Fig. SI4 in the Supp. Info. Thus, depending on the pressure, with modular surfaces the system might have to overcome two barriers, W $\rightarrow$ iC and iC $\rightarrow$ C, during the recovery process. The largest of the two barriers determines the recovery time. The dependence of the two barriers on the pressure might be different; for both modular surfaces the intrusion pressure is determined by the WiC barrier. Concerning the extrusion pressure, the relevant barrier is $\Delta\Omega^{\dagger}_{\mathrm{iCC}}$ for the square pore/pillar surface and $\Delta\Omega^{\dagger}_{\mathrm{WiC}}$ for the square pore/ridge one.

As expected, the square pore/pillar surface (Fig. 2e) presents a low W$\rightarrow$iC barrier, below 6.5 $k_{\mathrm{B}}T$ ($\phi_g = 0.03$), with a corresponding transition time of 7 ns (Table 2). However, at ambient conditions the intermediate Cassie-Baxter state is separated from the true Cassie-Baxter state by a barrier of 115.45 $k_{\mathrm{B}}T$, much lower than the single barrier of the system with only pillars, but still corresponding to the very large recovery times $\tau \sim 10^{39}$ s. This means that along the process the meniscus remains trapped at the intermediate Cassie-Baxter state and recovery takes place only at very negative pressures, $P^{\mathrm{ext}} = -7.1$ MPa. However, at these pressures the true Cassie-Baxter state is neither stable nor metastable, and the system evaporates[1].

[1]The Cassie-Baxter state for the pillar surface considered in this work is (meta)stable with respect to evaporation only up to $\sim -1MPa$

The iC $\rightarrow$ C barrier is associated to the depinning of the meniscus from the center of the edges of the pore. This suggests that reducing the number of edges, e.g., by combining the square pore with ridges, one could obtain a self-recovery surface without intermediate states (Fig. 2f). As expected, the modular square-pore/ridge surface presents no major differences from the square-pore/pillar and square-pore ones in the first part of the grand canonical potential profile, when the meniscus is within the pore. However, at variance with the square-pore/pillar surface, the barrier between the internal and external Cassie-Baxter states is negligible at ambient conditions, and the system is capable of full self-recovery. It is worth remarking that the for square-pore/ridge the intermediate Cassie-Baxter state exists only at pressures greater than ca. 3.5 MPa.

In summary, the modular square-pore/ridge surface combines self-recovery properties characterized by positive extrusion pressure ($P^{\text{ext}} = 2.0$ MPa, associated to the W$\rightarrow$iC step of the path) to good functional properties, e.g., an apparent contact angle of $\theta = 164°$. Further analysis shows that textured surfaces of this morphology can achieve self-recovery at ambient conditions up to a characteristic length of $S \sim 20$ nm (see Fig. SI5 of Supp. Info). This size is typically smaller than the one achievable for the fabrication of complex textures by *top down* approaches, such as photolithography.[56–58] To go beyond this limitation, in the future we plan to study textures of simpler fabrication based on the modular principles established in this work. Nevertheless, larger modular textures, within the range accessible by photolitography, enhance and facilitate the recovery with active approaches (see Fig. SI7). It must be remarked that novel specialized techniques[59] are very promising for the fabrication of nanoscopic textured surfaces and might be used to implement the modular design proposed here.

Comparison with molecular dynamics

The sharp-interface model adopted for modeling the continuum multiphase system implies a number of approximations which might affect the value of the wetting and recovery barriers,

especially at the nanoscale. Thus, to validate the results discussed above we have performed atomistic simulations of the recovery of the modular square-pore/ridge surface. The atomistic square-pore/ridge surface, shown in Fig. SI2, is obtained from a face-centered cubic crystal of Lennard-Jones (LJ) particles with a 0.36 nm lattice parameter. The solid particles interact with the oxygen atoms of the water molecules by a modified LJ potential, which allowed us to tune the Young contact angle of the material to the same value used in the continuum calculations. More details are given in the *Method* section. The atomistic texture pitch, thickness and hight are $S = 29$ atoms, $W = 6$ atoms and $H = 25$ atoms, of which 11 are relative to the pore. These correspond to slightly different values to those used in the previous section, namely $S = 10$ nm, $W = 2$ nm, and $H = 9$ nm, of which 4 nm are relative to the pore and 5 nm to the ridge. The direct comparison of atomistic results with continuum calculations in Fig. 3 has been performed using these latter values.

We prepared the system in the Wenzel state (Fig. 3a) and ran a constant pressure and temperature simulation at ambient conditions (further details in the *Method* section). Soon after the beginning of the simulation the gas fraction ϕ_{g} in the corrugation increases to values corresponding to the formation of a supercritical bubble, indicating the presence of a negligible recovery barrier, of the order of the thermal energy of the system, $k_{\mathrm{B}}T$. The recovery accelerates during the process ($\ddot{\phi}_{\mathrm{g}} > 0$) and, in agreement with continuum predictions, the system does not remain pinned at the internal Cassie-Baxter state. Finally, when the meniscus reaches the top of the ridges, ϕ_{g} shows damped oscillations resulting from the combined effect of inertia of the system, the pinning of the meniscus at the corners of ridges, and the viscosity of liquid.

To explain the recovery dynamics and draw a more direct comparison with the free-energy sharp-interface calculations we computed the *atomistic* free energy profile as a function of the liquid fraction by restrained molecular dynamics (see section *Methods* for details). Atomistic and sharp-interface results are consistent both from the point of view of the recovery mechanism (Fig. 3c-d) and of the energetics (Fig. 3b). For both models the recovery

starts with the formation of a gas bubble at a corner of the square pore. The bubble then spreads along the bottom corners of the pore one after the other, until it forms a circular bubble with the liquid touching the bottom wall at the center of the pore. The bubble grows further until it detaches from the bottom wall of the textures and the flat meniscus rises along the pore. Once at the top of the pore, the meniscus gets pinned at an intermediate position but the pinning force is very small and the recovery continues with an almost-flat meniscus moving up along the ridges until full recovery of the Cassie-Baxter state is achieved. Concerning the energetics, atomistic and sharp interface model Ω are in very good agreement (Fig. 3b), below the error of atomistic simulations. The atomistic model shows no metastable Wenzel state, i.e., there is no barrier between the Wenzel state, $\phi_{\mathrm{g}} = 0$, and the (internal or external) Cassie-Baxter one. This is a small difference from the sharp interface model, which predicts a small but non-zero barrier. Indeed, this is consistent with the known limitation of the sharp-interface model that cannot produce a (*strict*, i.e., barrierless) spinodal transition, both in bulk, heterogeneous, and confined systems.[60,61] In the present context this does not represent a severe limitation, rather it indicates that the recovery time predicted by our continuum calculations is an upper limit to the actual value. The absence of the Wenzel/Cassie-Baxter barrier makes it possible to have a prompt recovery (in the nanoseconds range) at ambient conditions for a pore/ridge surface of characteristic length $S = 10$ nm.

Summarizing, thanks to the separation between the region controlling the recovery – the intersection between the vertical features of the corrugation and bottom wall – and the zone determining the functional characteristics of the superhydrophobic surface – the top of corrugations – one can combine different texture morphologies into a modular surface with optimal functional and recovery characteristics. In particular, we have shown that ridges and square pores can be combined to produce self-recovery superhydrophobic surfaces with very high apparent contact angles.

Conclusions

In this work, we have investigated the wetting and recovery mechanism and energetics of a set of nanoscale textured surfaces with different morphologies. We have found that a nanoscopic size is a necessary but not sufficient condition for the wetting process to be reversible. Indeed, nanopillars and nanoridges cannot achieve self-recovery after being wet, i.e., there is no spontaneous recovery at ambient conditions on experimentally relevant timescales. On the contrary, pore structures, especially the one with square cross section, have very little recovery barrier and the process takes place readily. The reason for this different behaviour is related to the area of the hydrophobic solid exposed to the nucleating gas bubble which starts the recovery process. This solid/gas area of the nucleating bubble, which is maximum at the corner of the square pore, is the energetic gain balancing the penalty associated to the formation of a liquid/gas interface characteristic of the nucleus of the new phase.

The optimal morphology for self-recovery, the square pore, is sub-optimal for the functional properties of the surface, e.g., the contact angle or slippage. Considering that at ambient conditions the critical gas bubble starting the recovery in a square pore is rather small, with a volume of ~ 45 nm^3, $\phi_g = 0.046$, we propose a modular morphology, with a square pore combined with pillars or ridges. The pore/pillar surface presents an intermediate Cassie-Baxter state resulting from the pinning of the meniscus at the top of the pore. On the contrary, the pore/ridge surface does not present this problem and it is the optimal combination for self-recovery and functional properties. Self-recovery for such surfaces can be achieved for textures of up to 20 nm.

The results discussed above are based on the analysis of a sharp interface model of the three phase solid-liquid-gas system. These results have been validated by atomistic simulations of the pore/ridge system, which shows self-recovery on the atomistic timescale (2 ns). Indeed, the atomistic model of the three-phase system shows a barrier smaller than that predicted by the sharp interface model, suggesting that actual textured surfaces designed on the basis of the principles presented in this article might be more efficient at self-recovery

than estimated from our analysis.

Methods

CREaM

The wetting/recovery path is computed according to the continuum rare-event method (CREaM).[36] The CREaM path is the sequence of liquid/gas interfaces Σ_{lg} – the meniscus – at a set of values of the gas volume in the cavity $\phi_{\rm g}$ corresponding to the absolute constrained minimum (present value of $\phi_{\rm g}$) of the grand potential. In practice, CREaM is an extension of the classical nucleation theory (CNT[62–64]) to the case of vapor/liquid transition in a confined system. The numerical minimization of the constrained grand potential is obtained with the Surface Evolver code.[65] The input parameters for the three-phase system of Eq. (1) are the Young contact angle, $\theta_Y = 125°$, the surface tension of the liquid, $\gamma_{\rm lg} = 0.072$ N/m, and the difference between the liquid and gas pressures, which at ambient conditions is $\Delta P \approx 0.1$ MPa. As shown in Fig. 3, the morphology of the meniscus changes along the path, reflecting the change of the relative stability among the different bubble configurations as a function of $\phi_{\rm g}$.

Molecular dynamics simulations

Molecular dynamics (MD) simulations have been performed using the LAMMPS code.[66] Water molecules in the liquid and vapor phases are represented by the TIP4P/2015 model.[67] Their interaction with the walls is described by the modified Lennard-Jones (LJ) potential $v(r_{ab}) = 4\epsilon\left[(\sigma/r_{ab})^{12} - c\,(\sigma/r_{ab})^{6}\right]$, where r_{ab} is the distance between the oxygen atom of water molecules and the LJ atoms of the wall, ϵ and σ are the characteristic energy and length of the LJ interaction, respectively, and c is a parameter which is tuned to achieve the desired θ_Y (see Fig. SI1 in the Supp. Info.). In the present case $c = 0.75$, corresponding to $\theta = 124.8°$. The contact angle is measured by an independent MD simulation in which

we deposited and relaxed a large (diameter $\sim$ 6 nm) cylindrical sessile droplet over a flat surface.

The composite solid-liquid-vapor system is obtained by placing a slab of water molecules between a textured and flat surface oriented orthogonal to the z direction. Periodic boundary conditions are applied along the x ad y directions. The atoms of the textured surface are kept fixed during the simulation while the atoms of the flat surface are allowed to move only in the z direction. On the atoms of the flat surface is applied a constant force to keep the liquid at constant 0.1 MPa pressure. The system is kept at constant 300 K by a Nosé-Hoover chains thermostat.[68]

The atomistic Ω is computed by numerical integration of the mean force $\mathrm{d}\Omega/\mathrm{d}\phi$, which is obtained by restrained MD (RMD[40,69–71]). RMD consists in running simulations guided by an extended potential $v(\boldsymbol{r}) + \kappa/2(\phi_{\mathrm{g}}(\boldsymbol{r}) - \phi_{\mathrm{g}}^*)^2$, where $v(\boldsymbol{r})$ is the physical potential and $\kappa/2(\phi_{\mathrm{g}}(\boldsymbol{r}) - \phi_{\mathrm{g}}^*)^2$ is the restraining term forcing the system to visit configurations consistent with the condition $\phi_{\mathrm{g}}(\boldsymbol{r}) = \phi_{\mathrm{g}}^*$. Here $\phi_{\mathrm{g}}(\boldsymbol{r}) = (N_W - N(\boldsymbol{r}))/(N_W - N_{CB})$ is the atomistic estimate of the gas fraction in the textures, with $N(\boldsymbol{r})$ the number of water molecules in the textures at the present configuration $\boldsymbol{r}$, and N_W and N_{CB} number of molecules when the system is in the Wenzel and Cassie-Baxter state, respectively, and ϕ_{g}^* is the present target gas fraction. In the limit of large κ, $\mathrm{d}\Omega/\mathrm{d}\phi_{\mathrm{g}}^* = -\langle\kappa(\phi_{\mathrm{g}}(\boldsymbol{r}) - \phi_{\mathrm{g}}^*)\rangle_{\mathrm{RMD}}$, where $\langle\cdot\rangle_{\mathrm{RMD}}$ denotes average over the RMD simulation.[69]

Acknowledgement

The research leading to these results has received funding from the European Research Council under the European Union's Seventh Framework Programme (FP7/2007-2013)/ERC Grant agreement n. [339446]. We acknowledge PRACE for awarding us access to resource FERMI based in Italy at Casalecchio di Reno.

Supporting Information Available

Measurement of the atomistic contact angle; Structure of the atomistic modular textured surface; test of convergence of the atomistic mean force; some details of the calculation of free energy profiles via CREaM This material is available free of charge via the Internet at `http://pubs.acs.org/`.

References

1. Cassie, A.; Baxter, S. Wettability of Porous Surfaces. *Transactions of the Faraday Society* **1944**, *40*, 546–551.

2. Fürstner, R.; Barthlott, W.; Neinhuis, C.; Walzel, P. Wetting and Self-Cleaning Properties of Artificial Superhydrophobic Surfaces. *Langmuir* **2005**, *21*, 956–961.

3. Bhushan, B.; Jung, Y. C.; Koch, K. Micro-, Nano- and Hierarchical Structures for Superhydrophobicity, Self-Cleaning and Low Adhesion. *Philosophical Transactions of the Royal Society of London A: Mathematical, Physical and Engineering Sciences* **2009**, *367*, 1631–1672.

4. Cao, L.; Jones, A. K.; Sikka, V. K.; Wu, J.; Gao, D. Anti-Icing Superhydrophobic Coatings. *Langmuir* **2009**, *25*, 12444–12448.

5. Farhadi, S.; Farzaneh, M.; Kulinich, S. Anti-Icing Performance of Superhydrophobic Surfaces. *Applied Surface Science* **2011**, *257*, 6264–6269.

6. He, M.; Wang, J.; Li, H.; Song, Y. Super-Hydrophobic Surfaces to Condensed Micro-Droplets at Temperatures Below the Freezing Point Retard Ice/Frost Formation. *Soft Matter* **2011**, *7*, 3993–4000.

7. Samuel, J. J. S.; Ruther, P.; Frerichs, H.-P.; Lehmann, M.; Paul, O.; Rühe, J. A Simple

Route Towards the Reduction of Surface Conductivity in Gas Sensor Devices. *Sensors and Actuators B: Chemical* **2005**, *110*, 218–224.

8. Yamauchi, G.; Takai, K.; Saito, H. PTEE Based Water Repellent Coating for Telecommunication Antennas. *IEICE Transactions on Electronics* **2000**, *83*, 1139–1141.

9. Chen, C.-H.; Cai, Q.; Tsai, C.; Chen, C.-L.; Xiong, G.; Yu, Y.; Ren, Z. Dropwise Condensation on Superhydrophobic Surfaces With Two-Tier Roughness. *Applied Physics Letters* **2007**, *90*, 173108.

10. Rothstein, J. P. Slip on Superhydrophobic Surfaces. *Annual Review of Fluid Mechanics* **2010**, *42*, 89–109.

11. others,, *et al.* Structured Surfaces for a Giant Liquid Slip. *Physical Review Letters* **2008**, *101*, 064501.

12. Bidkar, R. A.; Leblanc, L.; Kulkarni, A. J.; Bahadur, V.; Ceccio, S. L.; Perlin, M. Skin-Friction Drag Reduction in the Turbulent Regime Using Random-Textured Hydrophobic Surfaces. *Physics of Fluids* **2014**, *26*, 085108–19.

13. Feng, L.; Zhang, Z.; Mai, Z.; Ma, Y.; Liu, B.; Jiang, L.; Zhu, D. A Super-Hydrophobic and Super-Oleophilic Coating Mesh Film for the Separation of Oil and Water. *Angewandte Chemie International Edition* **2004**, *43*, 2012–2014.

14. Zhou, X.; Zhang, Z.; Xu, X.; Guo, F.; Zhu, X.; Men, X.; Ge, B. Robust and Durable Superhydrophobic Cotton Fabrics for Oil/Water Separation. *ACS Applied Materials & Interfaces* **2013**, *5*, 7208–7214.

15. Li, J.; Shi, L.; Chen, Y.; Zhang, Y.; Guo, Z.; Su, B.-l.; Liu, W. Stable Superhydrophobic Coatings from Thiol-Ligand Nanocrystals and their Application in Oil/Water Separation. *Journal of Materials Chemistry* **2012**, *22*, 9774–9781.

16. Zhang, X.; Shi, F.; Niu, J.; Jiang, Y.; Wang, Z. Superhydrophobic Surfaces: from Structural Control to Functional Application. *Journal of Materials Chemistry* **2008**, *18*, 621–633.

17. Lifton, V. A.; Simon, S.; Frahm, R. E. Reserve Battery Architecture Based on Superhydrophobic Nanostructured Surfaces. *Bell Labs Technical Journal* **2005**, *10*, 81–85.

18. Li, W.; Wang, X.; Chen, Z.; Waje, M.; Yan, Y. Carbon Nanotube Film by Filtration as Cathode Catalyst Support for Proton-Exchange Membrane Fuel Cell. *Langmuir* **2005**, *21*, 9386–9389.

19. Zhang, F.; Zhao, L.; Chen, H.; Xu, S.; Evans, D. G.; Duan, X. Corrosion Resistance of Superhydrophobic Layered Double Hydroxide Films on Aluminum. *Angewandte Chemie International Edition* **2008**, *47*, 2466–2469.

20. Liu, T.; Yin, Y.; Chen, S.; Chang, X.; Cheng, S. Super-Hydrophobic Surfaces Improve Corrosion Resistance of Copper in Seawater. *Electrochimica Acta* **2007**, *52*, 3709–3713.

21. Wenzel, R. N. Resistance of Solid Surfaces to Wetting by Water. *Industrial & Engineering Chemistry* **1936**, *28*, 988–994.

22. Checco, A.; Ocko, B. M.; Rahman, A.; Black, C. T.; Tasinkevych, M.; Giacomello, A.; Dietrich, S. Collapse and Reversibility of the Superhydrophobic State on Nanotextured Surfaces. *Physical Review Letters* **2014**, *112*, 216101.

23. Amabili, M.; Giacomello, A.; Meloni, S.; Casciola, C. M. Intrusion and Extrusion of a Liquid on Nanostructured Surfaces. *Journal of Physics: Condensed Matter* **2016**, *29*, 014003–10.

24. Anslyn, E. V.; Dougherty, D. A. *Modern Physical Organic Chemistry*; University Science Books, 2006.

25. Blander, M.; Katz, J. L. Bubble Nucleation in Liquids. *AIChE Journal* **1975**, *21*, 833–848.

26. Lafuma, A.; Quéré, D. Superhydrophobic States. *Nature Materials* **2003**, *2*, 457–460.

27. Lee, C.; Kim, C.-J. C. Maximizing the Giant Liquid Slip on Superhydrophobic Microstructures by Nanostructuring their Sidewalls. *Langmuir* **2009**, *25*, 12812–12818.

28. Carlborg, C. F.; Do-Quang, M.; Stemme, G.; Amberg, G.; van der Wijngaart, W. Continuous Flow Switching by Pneumatic Actuation of the Air Lubrication Layer on Superhydrophobic Microchannel Walls. Micro Electro Mechanical Systems, 2008. MEMS 2008. IEEE 21st International Conference on. 2008; pp 599–602.

29. Carlborg, C. F.; Stemme, G.; van der Wijngaart, W. Microchannels with Substantial Friction Reduction at Large Pressure and Large Flow. Micro Electro Mechanical Systems, 2009. MEMS 2009. IEEE 22nd International Conference on. 2009; pp 39–42.

30. Li, Y.; Quéré, D.; Lv, C.; Zheng, Q. Monostable Superrepellent Materials. *Proceedings of the National Academy of Sciences* **2017**, *114*, 3387–3392.

31. Lee, C.; Kim, C.-J. Underwater Restoration and Retention of Gases on Superhydrophobic Surfaces for Drag Reduction. *Physical Review Letters* **2011**, *106*, 014502.

32. Manukyan, G.; Oh, J. M.; van den Ende, D.; Lammertink, R. G. H.; Mugele, F. Electrical Switching of Wetting States on Superhydrophobic Surfaces: A Route Towards Reversible Cassie-to-Wenzel Transitions. *Physical Review Letters* **2011**, *106*, 014501.

33. Boreyko, J. B.; Chen, C.-H. Restoring Superhydrophobicity of Lotus Leaves with Vibration-Induced Dewetting. *Physical Review Letters* **2009**, *103*, 174502.

34. Vrancken, R. J.; Kusumaatmaja, H.; Hermans, K.; Prenen, A. M.; Pierre-Louis, O.; Bastiaansen, C. W.; Broer, D. J. Fully Reversible Transition from Wenzel to Cassie-

Baxter States on Corrugated Superhydrophobic Surfaces. *Langmuir* **2009**, *26*, 3335–3341.

35. Zheng, Q.-S.; Yu, Y.; Zhao, Z.-H. Effects of Hydraulic Pressure on the Stability and Transition of Wetting Modes of Superhydrophobic Surfaces. *Langmuir* **2005**, *21*, 12207–12212.

36. Giacomello, A.; Chinappi, M.; Meloni, S.; Casciola, C. Metastable Wetting on Superhydrophobic Surfaces: Continuum and Atomistic Views of the Cassie-Baxter—Wenzel Transition. *Physical Review Letters* **2012**, *109*, 226102.

37. Papadopoulos, P.; Mammen, L.; Deng, X.; Vollmer, D.; Butt, H.-J. How Superhydrophobicity Breaks Down. *Proceedings of the National Academy of Sciences* **2013**, *110*, 3254–3258.

38. Lv, P.; Xue, Y.; Shi, Y.; Lin, H.; Duan, H. Metastable States and Wetting Transition of Submerged Superhydrophobic Structures. *Physical Review Letters* **2014**, *112*, 196101–5.

39. Lv, P.; Xue, Y.; Liu, H.; Shi, Y.; Xi, P.; Lin, H.; Duan, H. Symmetric and Asymmetric Meniscus Collapse in Wetting Transition on Submerged Structured Surfaces. *Langmuir* **2015**, *31*, 1248–1254.

40. Amabili, M.; Giacomello, A.; Meloni, S.; Casciola, C. M. Unraveling the Salvinia Paradox: Design Principles for Submerged Superhydrophobicity. *Advanced Materials Interfaces* **2015**, *2*.

41. Xue, Y.; Lv, P.; Lin, H.; Duan, H. Underwater Superhydrophobicity: Stability, Design and Regulation, and Applications. *Applied Mechanics Reviews* **2016**, *68*, 030803–39.

42. Bartolo, D.; Bouamrirene, F.; Verneuil, E.; Buguin, A.; Silberzan, P.; Moulinet, S. Bouncing or Sticky Droplets: Impalement Transitions on Superhydrophobic Micropatterned Surfaces. *EPL (Europhysics Letters)* **2006**, *74*, 299.

43. He, B.; Patankar, N. A.; Lee, J. Multiple Equilibrium Droplet Shapes and Design Criterion for Rough Hydrophobic Surfaces. *Langmuir* **2003**, *19*, 4999–5003.

44. Extrand, C. Designing for Optimum Liquid Repellency. *Langmuir* **2006**, *22*, 1711–1714.

45. Feng, X.; Jiang, L. Design and Creation of Superwetting/Antiwetting Surfaces. *Advanced Materials* **2006**, *18*, 3063–3078.

46. Butt, H.-J.; Semprebon, C.; Papadopoulos, P.; Vollmer, D.; Brinkmann, M.; Ciccotti, M. Design Principles for Superamphiphobic Surfaces. *Soft Matter* **2013**, *9*, 418–428.

47. Prakash, S.; Xi, E.; Patel, A. J. Spontaneous Recovery of Superhydrophobicity on Nanotextured Surfaces. *Proceedings of the National Academy of Sciences* **2016**, 201521753.

48. Giacomello, A.; Schimmele, L.; Dietrich, S.; Tasinkevych, M. Perpetual Superhydrophobicity. *Soft Matter* **2016**, *12*, 8927–8934.

49. Bonella, S.; Meloni, S.; Ciccotti, G. Theory and Methods for Rare Events. *The European Physical Journal B-Condensed Matter and Complex Systems* **2012**, *85*, 1–19.

50. Maragliano, L.; Vanden-Eijnden, E. A Temperature Accelerated Method for Sampling Free Energy and Determining Reaction Pathways in Rare Events Simulations. *Chemical Physics Letters* **2006**, *426*, 168–175.

51. Ybert, C.; Barentin, C.; Cottin-Bizonne, C.; Joseph, P.; Bocquet, L. Achieving Large Slip with Superhydrophobic Surfaces: Scaling Laws for Generic Geometries. *Physics of Fluids* **2007**, *19*, 123601.

52. Fadeev, A. Y.; McCarthy, T. J. Trialkylsilane Monolayers Covalently Attached to Silicon Surfaces: Wettability Studies Indicating that Molecular Topography Contributes to Contact Angle Hysteresis. *Langmuir* **1999**, *15*, 3759–3766.

53. others,, *et al.* An Evaluation of Methods for Contact Angle Measurement. *Colloids and Surfaces B: Biointerfaces* **2005**, *43*, 95–98.

54. Tsai, P.; Pacheco, S.; Pirat, C.; Lefferts, L.; Lohse, D. Drop Impact Upon Micro- and Nanostructured Superhydrophobic Surfaces. *Langmuir* **2009**, *25*, 12293–12298.

55. Seo, J.; García-Mayoral, R.; Mani, A. Pressure Fluctuations and Interfacial Robustness in Turbulent Flows over Superhydrophobic Surfaces. *Journal of Fluid Mechanics* **2015**, *783*, 448–473.

56. Shiu, J.-Y.; Kuo, C.-W.; Chen, P.; Mou, C.-Y. Fabrication of Tunable Superhydrophobic Surfaces by Nanosphere Lithography. *Chemistry of Materials* **2004**, *16*, 561–564.

57. Tuteja, A.; Choi, W.; Ma, M.; Mabry, J. M.; Mazzella, S. A.; Rutledge, G. C.; McKinley, G. H.; Cohen, R. E. Designing Superoleophobic Surfaces. *Science* **2007**, *318*, 1618–1622.

58. Gao, X.; Yan, X.; Yao, X.; Xu, L.; Zhang, K.; Zhang, J.; Yang, B.; Jiang, L. The Dry-Style Antifogging Properties of Mosquito Compound Eyes and Artificial Analogues Prepared by Soft Lithography. *Advanced Materials* **2007**, *19*, 2213–2217.

59. Checco, A.; Rahman, A.; Black, C. T. Robust Superhydrophobicity in Large-Area Nanostructured Surfaces Defined by Block-Copolymer Self Assembly. *Advanced Materials* **2014**, *26*, 886–891.

60. Oxtoby, D. W.; Evans, R. Nonclassical Nucleation Theory for the Gas–Liquid Transition. *The Journal of Chemical Physics* **1988**, *89*, 7521–7530.

61. Giacomello, A.; Chinappi, M.; Meloni, S.; Casciola, C. M. Geometry as a Catalyst: How Vapor Cavities Nucleate from Defects. *Langmuir* **2013**, *29*, 14873–14884.

62. Ford, I. Nucleation Theorems, the Statistical Mechanics of Molecular Clusters, and a Revision of Classical Nucleation Theory. *Physical Review E* **1997**, *56*, 5615.

63. Kalikmanov, V. *Nucleation Theory*; Springer, 2013; pp 17–41.

64. Oxtoby, D. W. Homogeneous Nucleation: Theory and Experiment. *Journal of Physics: Condensed Matter* **1992**, *4*, 7627.

65. Brakke, K. A. The Surface Evolver. *Experimental Mathematics* **1992**, *1*, 141–165.

66. Plimpton, S. Fast Parallel Algorithms for Short-Range Molecular Dynamics. *J. Comput. Phys.* **1995**, *117*, 1–19.

67. Abascal, J. L.; Vega, C. A General Purpose Model for the Condensed Phases of Water: TIP4P/2005. *J. Chem. Phys.* **2005**, *123*, 234505.

68. Martyna, G. J.; Klein, M. L.; Tuckerman, M. Nosé–Hoover Chains: the Canonical Ensemble *via* Continuous Dynamics. *The Journal of Chemical Physics* **1992**, *97*, 2635–2643.

69. Maragliano, L.; Vanden-Eijnden, E. A Temperature Accelerated Method for Sampling Free Energy and Determining Reaction Pathways in Rare Events Simulations. *Chem. Phys. Lett.* **2006**, *426*, 168–175.

70. Giacomello, A.; Meloni, S.; Chinappi, M.; Casciola, C. M. Cassie–Baxter and Wenzel States on a Nanostructured Surface: Phase Diagram, Metastabilities, and Transition Mechanism by Atomistic Free Energy Calculations. *Langmuir* **2012**, *28*, 10764–10772.

71. Meloni, S.; Giacomello, A.; Casciola, C. M. Theoretical Aspects of Vapor/Gas Nucleation at Structured Surfaces. *The Journal of Chemical Physics* **2016**, *145*, 211802.

Graphical TOC Entry